Journal of Advanced Ceramics
2022, **11**(4): 629–640
https://doi.org/10.1007/s40145-021-0564-0
ISSN 2226-4108
CN 10-1154/TQ

Research Article

Structure, defects, and microwave dielectric properties of Al-doped and Al/Nd co-doped $Ba_4Nd_{9.33}Ti_{18}O_{54}$ ceramics

Weijia GUO, Zhiyu MA, Yu LUO, Yugu CHEN, Zhenxing YUE*, Longtu LI

State Key Laboratory of New Ceramics and Fine Processing, School of Materials Science and Engineering, Tsinghua University, Beijing 100084, China

Received: August 9, 2021; Revised: December 6, 2021; Accepted: December 9, 2021

Abstract: Low-loss tungsten–bronze microwave dielectric ceramics are dielectric materials with potential application value for miniaturized dielectric filters and antennas in the fifth-generation (5G) communication technology. In this work, a novel Al/Nd co-doping method of $Ba_4Nd_{9.33}Ti_{18}O_{54}$ (BNT) ceramics with a chemical formula of $Ba_4Nd_{9.33+z/3}Ti_{18-z}Al_zO_{54}$ (BNT–AN, $0 \leqslant z \leqslant 2$) was proposed to improve the dielectric properties through structural and defect modulation. Together with Al-doped ceramics ($Ba_4Nd_{9.33}Ti_{18-z}Al_{4z/3}O_{54}$, BNT–A, $0 \leqslant z \leqslant 2$) for comparison, the ceramics were prepared by a solid state method. It is found that Al/Nd co-doping method has a significant effect on improving the dielectric properties compared with Al doping. As the doping amount z increased, the relative dielectric constant (ε_r) and the temperature coefficient of resonant frequency (τ_f) of the ceramics decreased, and the $Q\times f$ values of the ceramics obviously increased when $z \leqslant 1.5$. Excellent microwave dielectric properties of ε_r = 72.2, $Q\times f$ = 16,480 GHz, and τ_f = +14.3 ppm/℃ were achieved in BNT–AN ceramics with z = 1.25. Raman spectroscopy and thermally stimulated depolarization current (TSDC) technique were firstly combined to analyze the structures and defects in microwave dielectric ceramics. It is shown that the improvement on $Q\times f$ values was originated from the decrease in the strength of the A-site cation vibration and the concentration of oxygen vacancies ($V_O^{\cdot\cdot}$), demonstrating the effect and mechanism underlying for structural and defect modulation on the performance improvement of microwave dielectric ceramics.

Keywords: microwave dielectric ceramics; $Ba_4Nd_{9.33}Ti_{18}O_{54}$ (BNT); Al and Al/Nd doping; structural and defect modulation

1 Introduction

Nowadays, the fifth-generation (5G) telecommunication technology has been developing rapidly, in which ceramic materials could play important roles [1]. Microwave dielectric ceramics with high $Q\times f$ values (Q = 1/tanδ, and f is the resonant frequency) and excellent temperature stability are widely used to manufacture 5G antennas and filters [2–5]. In order to meet the requirements of device miniaturization, microwave dielectric ceramics having medium/high relative dielectric constants (ε_r) have been the focus of researches [6,7], including TiO_2 [8,9], $Ba_{6-3x}Ln_{8+2x}Ti_{18}O_{54}$ (BLT, where Ln = rare earth element) [10,11], $CaO–Li_2O–Ln_2O_3–TiO_2$ [12,13], $Ca_{1-x}Ln_{2x/3}TiO_3$ (CLT) [14–16], lead-based perovskite [17,18], etc. In recent years, BLT

* Corresponding author.
E-mail: yuezhx@mail.tsinghua.edu.cn

with a tungsten–bronze structure and CLT with a perovskite structure have been extensively studied [19–24]. Meanwhile, novel ceramic systems such as $Bi_2(Li_{0.5}Ta_{1.5})O_7$ [25,26] and $BiVO_4$ [27,28] have also been developed. However, the above-mentioned ceramic materials either have relatively low $Q\times f$ values or relatively large temperature coefficients of resonant frequency (τ_f), which cannot yet meet the application needs of 5G technology. It is necessary to develop microwave dielectric ceramics with better comprehensive performance.

The crystal structure of BLT ceramics is composed by three types of large cation sites: A1 rhombic sites, A2 pentagonal sites, and B sites (occupied by Ti^{4+}) in the center of TiO_6 octahedra [11]. According to Ohsato's report [11], Ln^{3+} and Ba^{2+} respectively occupy the A1 and A2 sites when x = 2/3, and the ordering of Ln^{3+} and Ba^{2+} reduces the internal strain and leads to the largest $Q\times f$ value. To further improve the $Q\times f$ values of BLT ceramics, a large amount of doping modification research was displayed, especially the substitution of low-valence cations for Ti^{4+} at the B sites. Chen *et al*. [29] and Tao *et al*. [30] replaced Ti^{4+} with the same amount of Al^{3+} to improve the $Q\times f$ value, while the condition of charge balance was not achieved. In order to meet the condition of charge balance, one method was to use composite ions such as $(Cr_{1/2}Nb_{1/2})^{4+}$, $(Mg_{1/3}Nb_{2/3})^{4+}$, or $(Al_{1/2}Nb_{1/2})^{4+}$ to substitute Ti^{4+} [31–33], yet it complicated the synthesis process. The other method is to use excessive trivalent cations (4/3 times in stoichiometry) such as Cr^{3+}, Al^{3+}, or Ga^{3+} to substitute Ti^{4+} [34–37], yet none of the studies have explained which site these cations entered. Considering that the A1 sites of BLT structure are usually not fully filled, the excessive cations might enter the A1 sites. However, the radii of those cations are much smaller than the size of the A1 sites, which might affect the stability of the crystal lattice and lead to the deterioration of the $Q\times f$ value. Therefore, it is important to conduct a further study on the ion occupancy during these doping process.

In the present study, $Ba_4Nd_{9.33}Ti_{18}O_{54}$ (BNT) ceramics ($\varepsilon_r \approx 85$, $Q\times f \approx 10{,}000$ GHz, and $\tau_f \approx +60$ ppm/℃) [11] are chosen as matrix. A new strategy, i.e., Al/Nd co-doping in BNT ceramics, is proposed to improve the dielectric properties of tungsten–bronze microwave dielectric ceramics through structural and defect modulation, in which the condition of charge balance was maintained by using the same amount of Al^{3+} to substitute Ti^{4+} and adding Nd^{3+} to fill the vacancies at the A1 site simultaneously, with a chemical formula of $Ba_4Nd_{9.33+z/3}Ti_{18-z}Al_zO_{54}$ (BNT–AN, $0 \leqslant z \leqslant 2$). Correspondingly, $Ba_4Nd_{9.33}Ti_{18-z}Al_{4z/3}O_{54}$ (BNT–A, $0 \leqslant z \leqslant 2$) ceramics are also prepared for comparison. The theoretical solid solubility should be reached when z = 2, at which the vacancies at the A1 site could be completely filled. Rietveld refinement, Raman spectroscopy, and thermally stimulated depolarization current (TSDC) are applied to analyze the crystal structure and the strength of the A-site cation vibration. Microwave dielectric ceramics with better comprehensive performance are obtained through Al/Nd co-doping, and the relationship between the structure and the microwave dielectric properties of the ceramics is discussed in the present paper.

2 Experimental

The BNT–A and BNT–AN ceramics were prepared through the traditional solid-state processing. High-purity powders including $BaCO_3$ (99.8%, Alfa Aesar), Nd_2O_3 (99.9%, Aladdin), TiO_2 (99.99%, Macklin), and Al_2O_3 (99.99%, Aladdin) were used as the raw materials. All the raw powders were calcined at 600 ℃ for 4 h, weighed according to the stoichiometric composition, and ball milled for 4 h in ethanol. After drying, the mixture was calcined at 1150 ℃ for 4 h, and then re-milled and dried. The dried powders were ground with polyvinyl alcohol solution (PVA, 5 wt%), and uniaxially pressed into cylinders with a diameter of 10 mm and an appropriate thickness. Finally, the specimens were preheated at 600 ℃ for 4 h to remove the binder and sintered in the range of 1350–1550 ℃ for 4 h.

The as-fired surfaces of the sintered ceramics were observed by scanning electron microscopy (SEM; MERLIN VP Compact, Carl Zeiss, Germany). The phase compositions and crystal structures of the ceramics were analyzed by X-ray diffraction (XRD; D8 Advance, Bruker, Karlsruhe, Germany) with Cu Kα radiation. Rietveld refinement were executed using the FullProf program [38] with XRD data collected over a 2θ range of 10°–120°. The bulk densities of the ceramics were determined by the Archimedes method, and the relative densities were calculated by the measured and theoretical ones. The ε_r and τ_f values at microwave range were measured using the Hakki–

Coleman method [39] by exciting the TE_{011} resonant mode [40] using a vector network analyzer (HP8720ES, Hewlett-Packard, Santa Rosa, USA). The $Q \times f$ values were measured using the $TE_{01\delta}$ mode in the cavity method [41]. Raman spectra (20–1200 cm^{-1}) of the ceramics were measured on a high-resolution Raman spectrometer (LabRAM HR800, Horiba Jobin-Yvon, France) with the existing line at 532 nm of a Nd/YAG laser at room temperature.

TSDC measurements were accomplished using a pA meter (6517B, Keithley, Cleveland, USA), and the temperature was controlled by a quarto temperature controller of Novocontrol Technologies (Montabaur, Germany). The ceramic pellets with diameter of ~8.4 mm and thickness of ~0.5 mm were polished, and gold electrodes were sputtered on both sides. The specimens were initially polarized under a DC electric field (E_p) at a constant temperature (T_p) for a period of time t_p (100 V/mm $\leqslant E_p \leqslant$ 350 V/mm, T_p = 300 ℃, and t_p = 10 min), and then rapidly cooled to −100 ℃ with E_p maintained to freeze the polarized defects. After E_p removed and being short-circuited for 10 min, the specimens were heated to 300 ℃ with a constant heating rate of 5 ℃/min, with the depolarization currents continually recorded.

3 Results and discussion

Figure 1 presents the SEM photographs of the surface morphology of the ceramic samples. All BNT–A and BNT–AN samples show a single phase of rod-like grains. As shown in Figs. 1(a)–1(c), BNT–A ceramics with different z values could be well-sintered at 1400 ℃. In comparison, BNT–AN ceramics with z = 2 are well-sintered at 1550 ℃, as shown in Fig. 1(f). The well-sintered samples are selected for subsequent characterization, and the sintering temperature of each composition is listed in Tables S1 and S2 in the Electronic Supplementary Material (ESM). According to Fig. 1 and Tables S1 and S2 in the ESM, it is indicated that the sintering temperature of the BNT–A ceramics is stable at around 1350–1400 ℃, while that of the BNT–AN ceramics is higher when z values are large. Figures 1(d) and 1(e) show that the grain size of the ceramics with the same composition becomes larger as the sintering temperature gets higher.

The XRD patterns of the ceramic samples are shown in Fig. 2. All samples can be confirmed as a single phase with a tungsten–bronze structure ($Ba_{3.99}Sm_{9.34}Ti_{18}O_{54}$, PDF#89-4356). The detailed XRD data with a 2θ range of 31°–35° are presented in Fig. 2(b), which shows that the peaks shift towards higher degrees as z value increases, indicating that the cell volume decreases. This demonstrates that Al^{3+} with a smaller ionic radius (0.54 Å, CN = 6) successfully enters into the lattice, and substitutes for Ti^{4+} with a larger ionic radius (0.605 Å, CN = 6). Rietveld refinement was performed to further explore the changes of phase composition and lattice parameters with doping amount. Figures 3(a)–3(c) show the refined results of the BNT, BNT–A (z = 1.25), and BNT–AN (z = 1.25) ceramics as examples, respectively. The fitting results are in good agreement with the experimental XRD patterns. Figure 3(d) shows

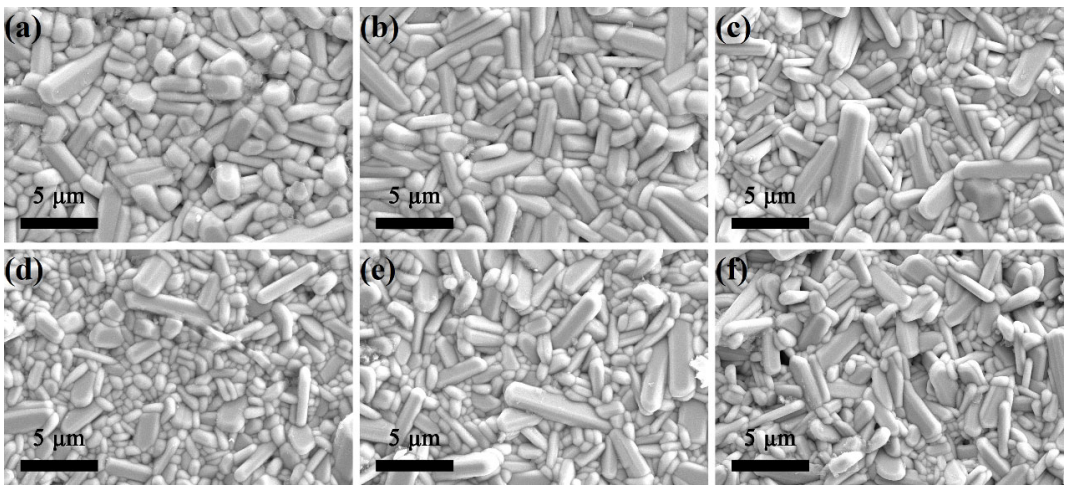

Fig. 1 SEM photographs of the BNT, BNT–A, and BNT–AN ceramics: (a) BNT, sintered at 1400 ℃; (b) BNT–A, z = 1.25, sintered at 1400 ℃; (c) BNT–A, z = 2, sintered at 1400 ℃; (d) BNT–AN, z = 1.25, sintered at 1400 ℃; (e) BNT–AN, z = 1.25, sintered at 1500 ℃; (f) BNT–AN, z = 2, sintered at 1550 ℃.

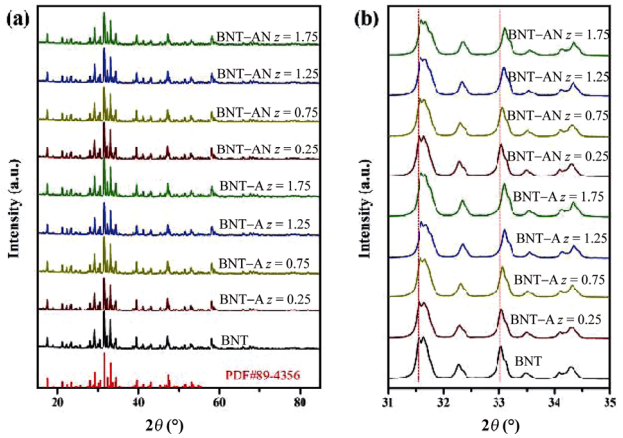

Fig. 2 (a) XRD patterns of the BNT, BNT–A, and BNT–AN ceramics (z = 0, 0.25, 0.75, 1.25, and 1.75). (b) XRD peak shifts in the range of 31° ⩽ 2θ ⩽ 35°.

that there are a few peaks that cannot be fitted in the experimental data of the BNT–A ceramics, together with χ^2 rising as z value increases, indicating that a small amount of unknown secondary phase appears. In contrast, Fig. 3(e) shows that there is no secondary phase peak in the experimental data of the BNT–AN ceramics. The above-mentioned unknown secondary phase may have an impact on the microwave dielectric properties of the BNT–A ceramics.

The lattice parameters and cell volumes calculated by Rietveld refinement are shown in Fig. 4. The lattice parameters and cell volumes of the BNT–A and BNT–AN ceramics both decrease with the increase in z value, and basically shows the same linear decrease trend as z ⩽ 1.25. This indicates that the type of trivalent cations (Al^{3+} or Nd^{3+}) filling the vacancies at the A1 sites has less influence on the lattice parameters in the doping process of the BNT ceramics. When z ⩾ 1.25, the lattice parameters and cell volumes of the BNT–AN ceramics continuously show a linear decreasing trend, while the decreasing trend of those of the BNT–A ceramics deviates from linearity. Combining with Figs. 3(d) and 3(e), it can be demonstrated that such a deviation is caused by the secondary phase in the BNT–A ceramics. Therefore, the BNT–A ceramics cannot form a complete solid solution phase when more Al^{3+} ions are added, while the BNT–AN ceramics can form a continuous solid solution in the range of 0 ⩽ z ⩽ 2. The detailed results of the structural parameters and reliability factors obtained by Rietveld refinement are shown in Tables S1 and S2 in the ESM.

Figure 5 presents the relative densities and microwave dielectric properties of the BNT–A and BNT–AN ceramics. According to Fig. 5(a), the relative densities of almost all ceramic samples have reached higher than 97%, indicating the ceramics are all well densified. When

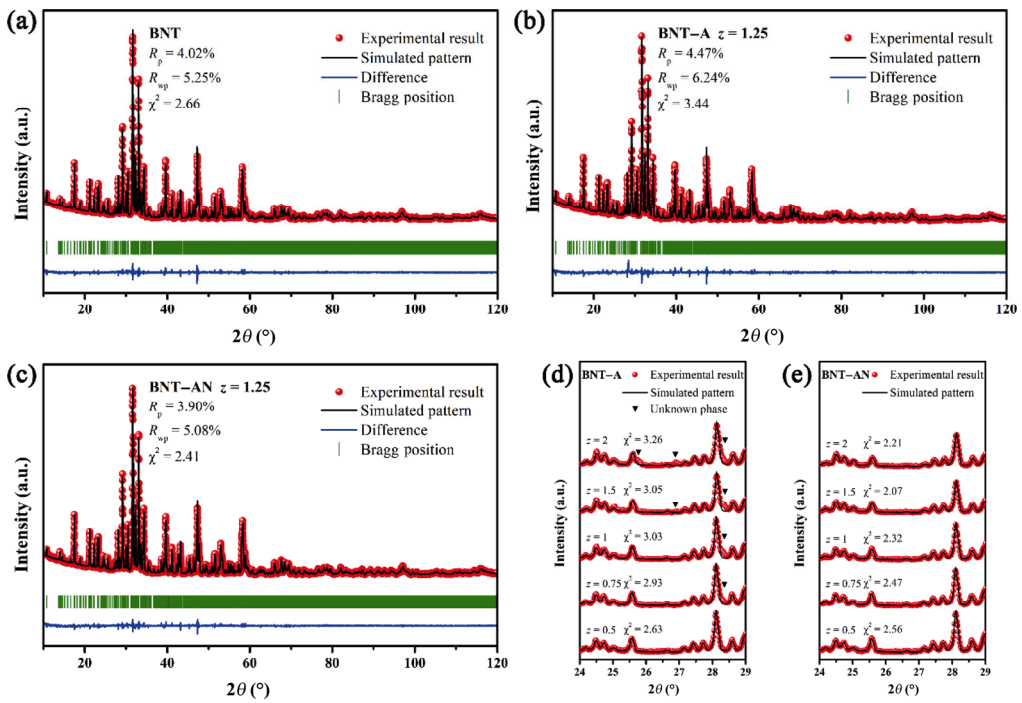

Fig. 3 Rietveld refinement results of (a) the BNT ceramics, (b) the BNT–A (z = 1.25) ceramics, and (c) the BNT–AN (z = 1.25) ceramics; detailed Rietveld refinements results of (d) the BNT–A (0.5 ⩽ z ⩽ 2) ceramics and (e) the BNT–AN (0.5 ⩽ z ⩽ 2) ceramics.

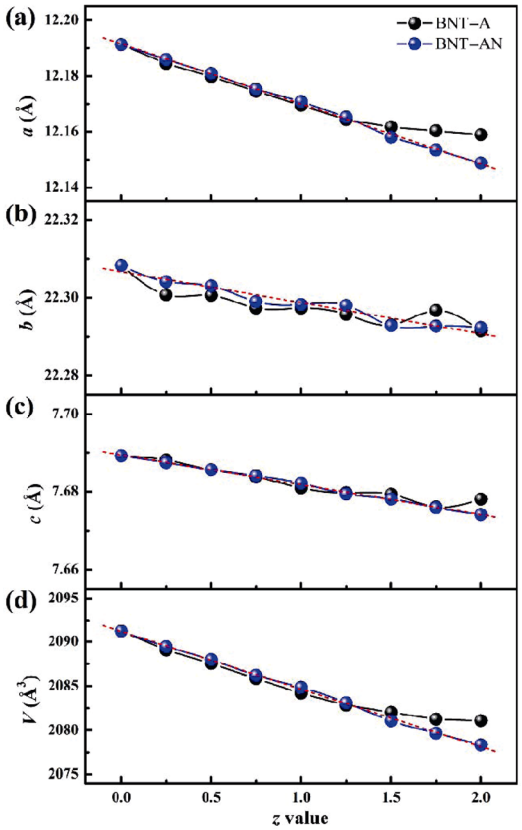

Fig. 4 Lattice parameters (a) a, (b) b, (c) c, and (d) the cell volume of the BNT–A and BNT–AN ($0 \leqslant z \leqslant 2$) ceramics.

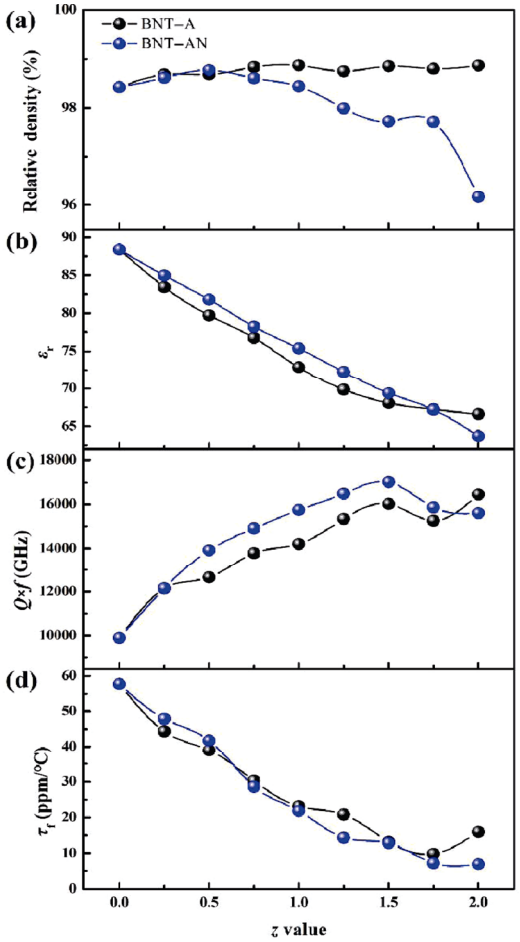

Fig. 5 (a) Relative densities, (b) ε_r values, (c) $Q\times f$ values, and (d) τ_f values of the BNT–A and BNT–AN ($0 \leqslant z \leqslant 2$) ceramics.

$z \geqslant 1$, the relative densities of the BNT–AN ceramics are lower than those of BNT–A ceramics with the same doping amount. In addition, the sintering temperature of the BNT–AN ceramics is higher with large z values as illustrated in SEM results. Therefore, the BNT–AN ceramics are more difficult to be well-sintered than the BNT–A ceramics. Figures 5(b) and 5(d) show that the ε_r and τ_f values of the ceramics decrease in a similar trend with the increase in z value, which is consistent with the reports of low-valence cations doping at the B sites in the BLT system [29–37]. According to Shannon's rule [42], ε_r is related to the ionic polarizability (α_D) and the molecular volume (V_m):

$$\alpha_D = \frac{V_m(\varepsilon_{rc}-1)}{b(\varepsilon_{rc}+2)} \quad (1)$$

where ε_{rc} is the corrected dielectric constant, and b is a constant equal to $4\pi/3$. According to Eq. (1), ε_{rc} increases when α_D increases or V_m decreases. Although the cell volume of the ceramics decreases slightly when z value increases as shown in Fig. 4, the decrease in α_D ($\alpha(Al^{3+}) = 0.78$ Å^3, $\alpha(Ti^{4+}) = 2.94$ Å^3) mainly dominates the decrease in ε_r. Reaney and Iddles [6] reported that τ_f is usually determined by ε_r, and the change trends of ε_r and τ_f are often similar in the same ceramic system. When $z \geqslant 1.25$, the decrease in ε_r of the BNT–A ceramics slows down, and it is related to the small amount of secondary phase, consistent with the previous results of Al-doping in the BLT system [36]. Figure 5(c) shows that when $z \leqslant 1.5$, the $Q\times f$ values of the ceramics significantly increase as z value increases, which may be related to the decline in the activity of $V_O^{\cdot\cdot}$ illustrated by TSDC technique in our past research [36]. As $z \geqslant 1.5$, the continuous doping makes the $Q\times f$ values of the ceramics decrease slightly. It can be indicated that the decrease in the $Q\times f$ values of the BNT–A ceramics is affected by the secondary phase, and that of BNT–AN ceramics is related to the decline of densification. BNT–AN ceramics with $z = 1.25$ have reached excellent microwave dielectric properties: $\varepsilon_r = 72.2$, $Q\times f = 16{,}480$ GHz, and $\tau_f = +14.3$ ppm/℃.

It is noticed from Figs. 5(b) and 5(c) that when $z \leqslant 1.5$, the ε_r and $Q\times f$ values of the BNT–AN ceramics are both higher than those of the BNT–A ceramics with the same doping amount, indicating that Al/Nd co-doping is a superior strategy for the substitution in the BNT ceramics. The comparison of the ε_r and $Q\times f$ values of these ceramics is visually presented in Fig. 6. This important difference in microwave dielectric properties may be related to the factors such as the composition, structure, and defects of the ceramics. The trivalent cations filling the vacancies at the A1 sites have different polarizabilities ($\alpha(Al^{3+}) = 0.78$ Å^3, $\alpha(Nd^{3+}) = 5.01$ Å^3), which results in higher ε_r values of BNT–AN ceramics according to Shannon's rule [42]. As for the $Q\times f$ values, the determinants may become more complicated: In addition to the secondary phase and porosity that have been discussed, the defects and stability of crystal lattice may also play an important role [6,43]. Bond length, bond valence, and bond energy are important factors that reflect the stability of crystal lattice, and have been used to explore the relationship between the structure and properties of microwave dielectric properties [44–46]. However, according to the results of Rietveld refinement, the variation of the average bond length of the ceramics related to z value is less than 0.01 Å, which is roughly equivalent to the uncertainty of Rietveld refinement method (~0.006 Å). The average bond length of A1–O is shown in Fig. S1 in the ESM as an example. These data could hardly be used for further analysis. Therefore, Raman spectroscopy and TSDC technique are performed to further explore the relationship among the crystal structure, defects, and $Q\times f$ values of the ceramics.

Raman spectroscopy can reflect the lattice vibration information of the materials. The polarization mechanism of dielectrics in the microwave frequency band is mainly ion displacement polarization [47], which is closely related to the vibration of ions in the crystal lattice. Therefore, Raman spectroscopy is a powerful tool for studying the relationship between the structure and properties of microwave dielectric ceramics [21,33,48–54]. The space group of the BLT superlattice with tungsten–bronze structure is *Pbnm* (No. 62), and there are 24 Raman active vibration modes: $7A_g + 7B_g + 5B_{2g} + 5B_{3g}$ [55]. The Raman spectrum results of the BNT–A and BNT–AN ceramics are presented in Fig. 7. A total of 17 Raman vibration modes were observed in the experimental data. As the Raman spectra of the BLT system are excessively complex, previous studies had different opinions on the identification of Raman modes. Nevertheless, most studies considered that the Raman vibration modes in the region of 100–200 cm^{-1} correspond to A-site cation translation. The vibration modes in the regions of 200–400 and 400–600 cm^{-1} were attributed to the rotation and the internal vibration of the TiO_6 octahedra, respectively. The mode at 757 cm^{-1} might correspond to the second order scatter [21,33,52–54]. Limited by the test conditions, vibration modes between 50 and 100 cm^{-1} in the BLT system have not been reported yet. Previous studies on perovskite systems such as $SmAlO_3$, $NdNiO_3$, $LaGaO_3$, and $BaCeO_3$, which also have the space group symmetry *Pbnm*, reported Raman modes in the region of 50–100 cm^{-1}, and identified all those modes as A-site cation translation [55–60]. Therefore, in the BNT–A and BNT–AN systems, the vibration modes between 50 and 100 cm^{-1} are identified as A-site cation translation as well as the vibration modes between 100 and 200 cm^{-1}. It is reported that the mode at 234 cm^{-1} was considered as the tilting vibration of the TiO_6 octahedra when the A sites are occupied by

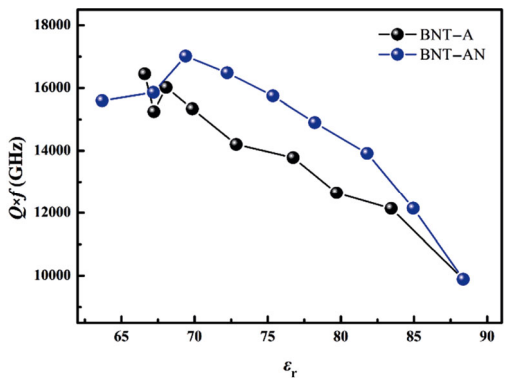

Fig. 6 ε_r and $Q\times f$ values of the BNT–A and BNT–AN ($0 \leqslant z \leqslant 2$) ceramics.

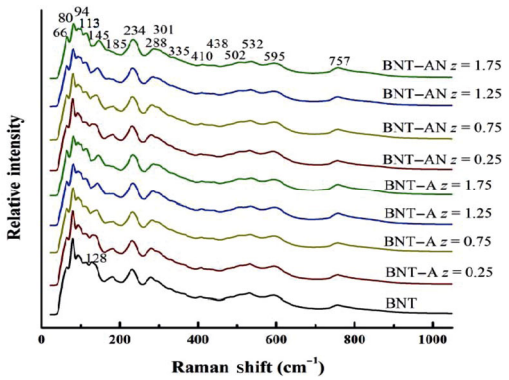

Fig. 7 Raman spectra of the BNT–A and BNT–AN (z = 0, 0.25, 0.75, 1.25, and 1.75) ceramics.

Ba^{2+} [49,55]. The doping methods in the present work have not made any changes to the Ba^{2+} cations occupying the A2 sites, so it can be considered that this mode does not change significantly. In order to compare the intensities of the Raman modes, the relative intensities of the Raman spectra in Fig. 7 were obtained by normalizing the experimental intensities based on the peak values of the Raman mode at 234 cm^{-1}.

As shown in Fig. 7, with the increase in z value, most of the Raman modes present a blue-shift, which indicates that the cell volume decreases [21,33,47,50, 53,54,61], consistent with the XRD results. The relative intensities of the vibration modes in the region of 300–400 cm^{-1} increase slightly as z value increases, implying that the tilting vibration of the TiO_6 octahedra becomes stronger, and the decline of τ_f is related to this phenomenon [49,52,54]. More obvious changes appear in the vibration modes between 50 and 200 cm^{-1}, which are identified as A-site cation translation. As z value increases, the relative intensities of these Raman modes are significantly reduced, where the variation of relative intensities of the Raman modes at 80 and 94 cm^{-1} is shown in Fig. 8 as an example. It represents that the A-site cation translation is weakened, indicating that the binding force towards the A-site cations is strengthened, and accordingly the contribution to the microwave dielectric loss is reduced and the $Q\times f$ values increase. Comparing the Raman spectra of BNT–A and BNT–AN ceramics with the same z value, it is found that the relative intensities of the Raman modes at 80 and 94 cm^{-1} of the BNT–AN ceramics are lower than those of the BNT–A ceramics, as shown in Fig. 8. It is implied that the strength of the A-site cation vibration in the BNT–AN ceramics is weaker, so the contribution to the microwave dielectric loss is lower, and the $Q\times f$ values are higher. Briefly, the relationship between the $Q\times f$ values and the strength of the A-site cation vibration in the BNT–A and BNT–AN systems has been established through Raman spectroscopy.

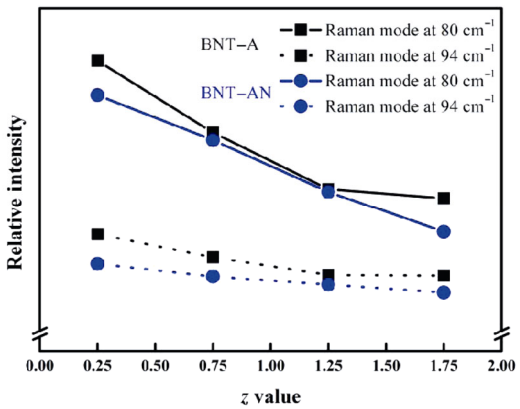

Fig. 8 Relative intensities of Raman modes at 80 and 94 cm^{-1} of the BNT–A and BNT–AN (z = 0.25, 0.75, 1.25, and 1.75) ceramics.

TSDC technique can provide valuable information on the types and concentrations of defects in dielectrics, and has been widely used to explore the dielectric response mechanism of ceramics [36,62–69]. Liu and Randall [62] firstly reported the method for determining the types of defects in inorganic dielectrics through the changes in peak position (T_m, the temperature at which the absolute value of current density is maximized) and peak intensity (J_m, the maximum of the absolute value of current density) of the TSDC curves with various polarization conditions (T_p and E_p), and Zhang *et al.* [67] applied this method to microwave dielectric ceramics for the first time. Figure 9 shows the TSDC curves of the BNT, BNT–A (z = 1.25), and BNT–AN (z = 1.25) ceramics. The curves of all samples show three or four TSDC peaks, indicating that there are at least three or four defect relaxation mechanisms. In the range of 50 ℃ < T_m < 150 ℃, there is a weak peak (referred to as peaks A_1, A_2, and A_3) in each figure. And peaks similar to each other (referred to as peaks B_1, B_2, and B_3) are displayed in the range of 160 ℃ < T_m < 200 ℃. The TSDC curves of different samples are quite different in the high temperature section above 200 ℃. The curves of the undoped sample exhibit a very strong peak (referred to as peak D_1), and its T_m values have exceeded the test range. The curves of the two doped samples both show peaks with similar changes (referred to as peaks C_2 and C_3) at around 240 ℃. The TSDC curves of the BNT–A (z = 1.25) ceramics also show a weak peak (referred to as peak D_2) with T_m > 280 ℃.

The T_m and J_m of peaks A_1 and A_3 both increase with an increase in E_p, indicating that these peaks are related to the relaxation of $V_O^{\cdot\cdot}$. As E_p increases, the J_m of peak A_2 increases while the T_m decreases, indicating that peak A_2 is related to the relaxation of trapped charges. Using the initial rise method [67,70], the activation energies of peaks A_1, A_2, and A_3 are calculated as 0.43–0.50, 0.14–0.17, and 0.24–0.36 eV, respectively. Based on the previous results from Refs. [36,65,66], the activation energies of peaks A_1 and A_3 are close to those of the in-grain $V_O^{\cdot\cdot}$, and it can be inferred that these peaks are related to the relaxation of the in-grain $V_O^{\cdot\cdot}$. The T_m and activation energy of peak

A_2 are similar to those of peaks A_1 and A_3, and it is speculated that peak A_2 may correspond to trap charges associated with the in-grain $V_O^{\cdot\cdot}$. Peaks B_1, B_2, B_3, C_2, and C_3 have T_m values which basically unchanged with polarization conditions, while their J_m values increase with an increase in E_p, indicating that they are related to the relaxation of defect dipoles. The calculated activation energies of peaks B_1, B_2, and B_3 are 0.58–0.80, 0.64–0.75, and 0.59–0.75 eV, respectively. According to the results from Refs. [36,64,71], it can be inferred that peak B is related to the relaxation of the $Ti'_{Ti} - V_O^{\cdot\cdot}$ defect dipoles. Although the activation energies of peaks C_2 and C_3 are difficult to calculate by the initial rise method, the type of defects related to peak C could be determined by the defect reactions in the doping process, considering that peak C appears only after doping. During the substitution process of Al^{3+} for Ti^{4+} at the B sites, Al'_{Ti} point defects are formed. Meanwhile, excess trivalent cations (Al^{3+} or Nd^{3+}) were added to fill the vacancies at the A1 sites, forming $Al_{A1}^{\cdot\cdot\cdot}$ or $Nd_{A1}^{\cdot\cdot\cdot}$ point defects. Thus the condition of charge balance could be ensured, without ion valence changing or $V_O^{\cdot\cdot}$ producing. Therefore, peaks C_2 and C_3 are considered as the relaxation peaks of the $Al'_{Ti} - Al_{A1}^{\cdot\cdot\cdot}$ and $Al'_{Ti} - Nd_{A1}^{\cdot\cdot\cdot}$ defect dipoles, respectively. As for peak D_1, the current density rises slower when E_p is higher, indicating that it will reach a peak value at a higher temperature with higher E_p, which signifies that peak D_1 is related to the relaxation of $V_O^{\cdot\cdot}$. The calculated activation energy of peak D_1 is 0.98–1.19 eV, similar to that of the across-grain-boundary $V_O^{\cdot\cdot}$ (1.1 eV) [36,63]. It is implied that peak D_1 is related to the relaxation of the across-grain-boundary $V_O^{\cdot\cdot}$. Since the position of peak D_2 is similar to that of peak D_1, it is speculated that the relaxation mechanisms of the two are the same, so that it can be considered that peak D_2 is also related to the relaxation of the across-grain-boundary $V_O^{\cdot\cdot}$.

TSDC peaks with higher J_m imply a higher concentration of the corresponding defects [69,72]. Comparing the TSDC curves of the three ceramic samples, the BNT ceramics with peak D_1 in Fig. 9(a) show extremely high concentration of the across-grain-boundary $V_O^{\cdot\cdot}$, while the BNT–A (z = 1.25) ceramics with peak D_2 in Fig. 9(b) show only a small amount of the across-grain-boundary $V_O^{\cdot\cdot}$, and the BNT–AN (z = 1.25) ceramics show no peaks corresponding to the across-grain-boundary $V_O^{\cdot\cdot}$ in Fig. 9(c). It is generally believed that oxygen vacancies could cause the extrinsic

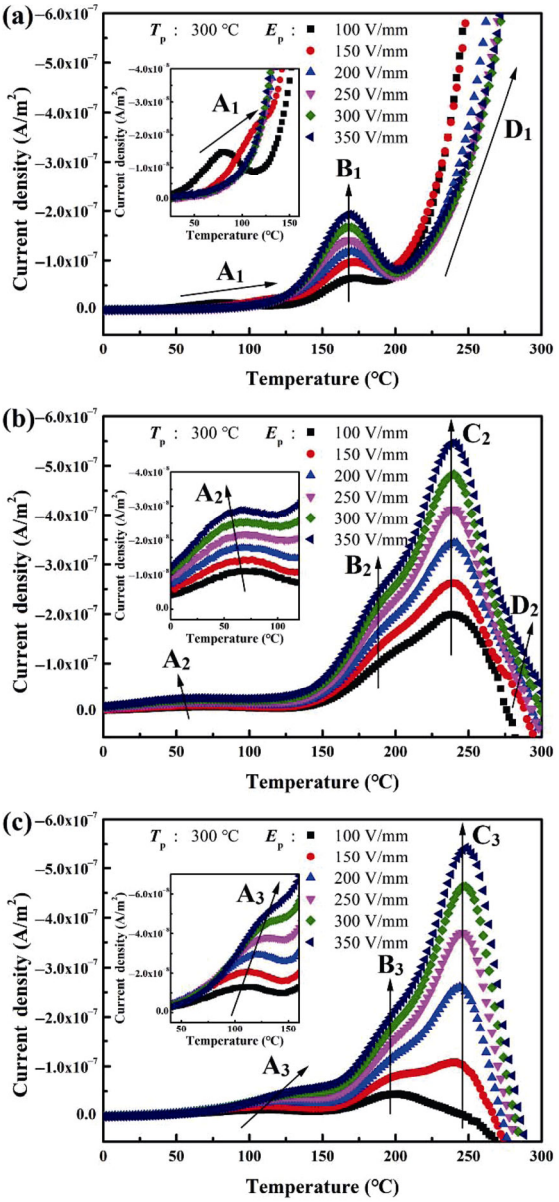

Fig. 9 TSDC curves of (a) the BNT ceramics, (b) the BNT–A (z = 1.25) ceramics, and (c) the BNT–AN (z = 1.25) ceramics under T_p = 300 ℃ and 100 V/mm ⩽ E_p ⩽ 350 V/mm.

loss of dielectric ceramics, and affect the $Q \times f$ values at microwave frequency bands [6]. The TSDC results in the present work are consistent with it. It is noticed that each O^{2-} in the crystal lattice is adjacent to several A-site cations in the BLT system. Associating the results of TSDC with the aforementioned Raman spectroscopy of the BNT–A and BNT–AN ceramics, it can be found that with the strengthening of binding force between the A-site cations and O^{2-}, the formation of $V_O^{\cdot\cdot}$ becomes difficult, indicating that the results of TSDC and Raman spectroscopy are consistent. It is demonstrated

for the first time that in the structural and defect modulation of the BNT ceramics, the formation of $V_O^{\cdot\cdot}$ in the crystal lattice is closely related to the strength of the A-site cation vibration, $V_O^{\cdot\cdot}$ affects the lattice vibration, and then affects the microwave dielectric loss.

The microwave dielectric properties ($Q\times f$ value vs. ε_r) of medium/high ε_r ceramics reported after 2010 with high Q and near-zero τ_f are summarized in Fig. 10 [25,26,29,33,36,37,54,73–78]. The current BNT–AN ceramics obviously exhibit superior microwave dielectric properties. Using the structural and defect modulation strategy, the novel doping strategy developed in this paper could provide new ways on the modification of medium/high ε_r ceramics, and the ceramics could have outstanding application prospects in the 5G technology.

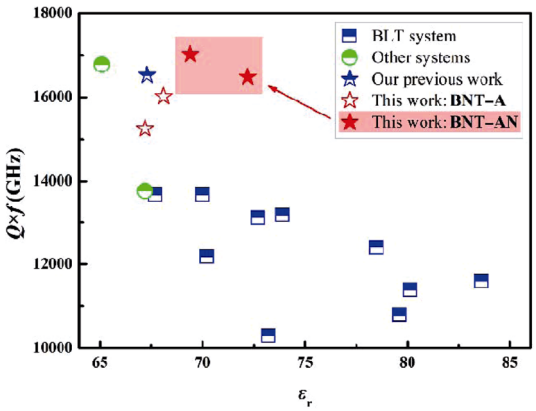

Fig. 10 Summary of $Q\times f$ value vs. ε_r plot for microwave dielectric ceramics reported after 2010 with $65 < \varepsilon_r < 85$, $Q\times f > 10{,}000$ GHz, and -20 ppm/℃ $< \tau_f < 20$ ppm/℃. The data are collected from Refs. [25,26,29,33,36,37,54, 73–78].

4 Conclusions

The Al-doped and Al/Nd co-doped BNT ceramics are prepared through the solid state processing. The microwave dielectric properties of the BNT–A and BNT–AN ceramics are compared, and the relationship among the composition, structure, defects, and microwave dielectric properties of the ceramics was explored through Rietveld refinement, Raman spectroscopy, and TSDC technique. As the doping amount increases, the ε_r and τ_f values of the ceramics decrease, and the $Q\times f$ values first increase and then slightly decrease. The ε_r and $Q\times f$ values of BNT–AN ceramics are both higher than those of BNT–A ceramics, indicating that Al/Nd co-doping is a novel and superior doping method that maintains the condition of charge balance. The results of Rietveld refinement show that there is a small amount of unknown secondary phase in the BNT–A ceramics, and the relative density data show that the BNT–AN ceramics are more difficult to densify, which may result in the deterioration of microwave dielectric performance when $z \geqslant 1.5$. Raman spectroscopy and TSDC measurement together show that the $Q\times f$ values of the BNT–A and BNT–AN ceramics are closely related to the strength of the A-site cation vibration and the concentration of $V_O^{\cdot\cdot}$. With the strengthening of binding force between the A-site cations and O^{2-}, the contribution of the A-site cations to the microwave dielectric loss reduces, the $Q\times f$ values decrease, and the formation of $V_O^{\cdot\cdot}$ becomes difficult. It is also proved that in microwave frequency bands, oxygen vacancies affect the dielectric loss by affecting the lattice vibration. Microwave dielectric ceramics with excellent performance in the field of medium/high ε_r were obtained by the structural and defect modulation strategy: $\varepsilon_r = 72.2$, $Q\times f = 16{,}480$ GHz, and $\tau_f = +14.3$ ppm/℃, which could have outstanding application prospects in the 5G technology.

Acknowledgements

This work was supported by the National Key R&D Program of China (No. 2017YFB0406301), the Key-Area Research and Development Program of Guangdong Province (No. 2020B010176001), and the National Natural Science Foundation of China (No. 51872160).

Electronic Supplementary Material

Supplementary material is available in the online version of this article at https://doi.org/10.1007/s40145-021-0564-0.

References

[1] Hill MD, Cruickshank DB, MacFarlane IA. Perspective on ceramic materials for 5G wireless communication systems. *Appl Phys Lett* 2021, **118**: 120501.

[2] Jin DH, Hu CC, Liu B. Improved sinterability and temperature stability in Zn^{2+}/Ti^{4+}-co-substituted $CaAl_2O_4$ ceramics and their 5G antenna applications. *J Mater Sci Mater Electron* 2021, **32**: 18205–18211.

[3] Zhang L, Zhang J, Yue ZX, *et al*. Thermally stable polymer–ceramic composites for microwave antenna applications. *J Adv Ceram* 2016, **5**: 269–276.

[4] Medeiros JLG, d'Assunção AG, Mendonça LM. Microstrip

fractal patch antennas using high permittivity ceramic substrate. In: Proceedings of the 2012 IEEE International Symposium on Antennas and Propagation, Chicago, USA, 2012: 1–2.

[5] Rhbanou A, El F, Jebbor N, *et al*. New design of miniature C-band substrate integrated waveguide bandpass filters using ceramic material. *FME Trans* 2021, **49**: 103–112.

[6] Reaney IM, Iddles D. Microwave dielectric ceramics for resonators and filters in mobile phone networks. *J Am Ceram Soc* 2006, **89**: 2063–2072.

[7] Yang HC, Zhang SR, Yang HY, *et al*. The latest process and challenges of microwave dielectric ceramics based on pseudo phase diagrams. *J Adv Ceram* 2021, **10**: 885–932.

[8] Cohn SB. Microwave bandpass filters containing high-Q dielectric resonators. *IEEE Trans Microw Theory Tech* 1968, **16**: 218–227.

[9] Zhao ED, Hao JY, Xue X, *et al*. Rutile TiO_2 microwave dielectric ceramics prepared via cold sintering assisted two step sintering. *J Eur Ceram Soc* 2021, **41**: 3459–3465.

[10] Ohsato H, Ohhashi T, Nishigaki S, *et al*. Formation of solid solutions of new tungsten bronze-type microwave dielectric compounds $Ba_{6-3x}R_{8+2x}Ti_{18}O_{54}$ (R = Nd and Sm, $0 \leqslant x \leqslant 1$). *Jpn J Appl Phys* 1993, **32**: 4323–4326.

[11] Ohsato H. Science of tungstenbronze-type like $Ba_{6-3x}R_{8+2x}Ti_{18}O_{54}$ (R = rare earth) microwave dielectric solid solutions. *J Eur Ceram Soc* 2001, **21**: 2703–2711.

[12] Ezaki K, Baba Y, Takahashi H, *et al*. Microwave dielectric properties of $CaO–Li_2O–Ln_2O_3–TiO_2$ Ceramics. *Jpn J Appl Phys* 1993, **32**: 4319–4322.

[13] Zhou CR, Chen GH, Cen ZY, *et al*. Structure and microwave dielectric characteristics of lithium-excess $Ca_{0.6}Nd_{0.8/3}TiO_3/(Li_{0.5}Nd_{0.5})TiO_3$ ceramics. *Mater Res Bull* 2013, **48**: 4924–4929.

[14] Yoshida M, Hara N, Takada T, *et al*. Structure and dielectric properties of $(Ca_{1-x}Nd_{2x/3})TiO_3$. *Jpn J Appl Phys* 1997, **36**: 6818–6823.

[15] Kim WS, Kim ES, Yoon KH. Effects of Sm^{3+} substitution on dielectric properties of $Ca_{1-x}Sm_{2x/3}TiO_3$ ceramics at microwave frequencies. *J Am Ceram Soc* 1999, **82**: 2111–2115.

[16] Huang CL, Tsai JT, Chen YB. Dielectric properties of $(1-y)Ca_{1-x}La_{2x/3}TiO_3–y(Li,Nd)_{1/2}TiO_3$ ceramic system at microwave frequency. *Mater Res Bull* 2001, **36**: 547–556.

[17] Kato J, Kagata H, Nishimoto K. Dielectric properties of $(PbCa)(MeNb)O_3$ at microwave frequencies. *Jpn J Appl Phys* 1992, **31**: 3144–3147.

[18] Kucheiko S, Choi JW, Kim HJ, *et al*. Microwave characteristics of $(Pb,Ca)(Fe,Nb,Sn)O_3$ dielectric materials. *J Am Ceram Soc* 1997, **80**: 2937–2940.

[19] Huang XP, Liu XY, Liu F, *et al*. Microstructures and microwave dielectric properties of $(Ba_{1-x}Sr_x)_4(Sm_{0.4}Nd_{0.6})_{28/3}Ti_{18}O_{54}$ solid solutions. *J Adv Ceram* 2017, **6**: 50–58.

[20] He TC, Lv CH, Li WH, *et al*. The dielectric constant of $Ba_{6-3x}(Sm_{1-y}Nd_y)_{8+2x}Ti_{18}O_{54}$ (x = 2/3) ceramics for microwave communication by linear regression analysis. *Materials* 2020, **13**: 5733.

[21] Wang G, Fu QY, Guo PJ, *et al*. Crystal structure, spectra analysis and dielectric characteristics of $Ba_4M_{28/3}Ti_{18}O_{54}$ (M = La, Pr, Nd, and Sm) microwave ceramics. *Ceram Int* 2021, **47**: 1750–1757.

[22] Chen YG, Guo WJ, Luo Y, *et al*. Microwave and terahertz properties of porous $Ba_4(Sm,Nd,Bi)_{28/3}Ti_{18}O_{54}$ ceramics obtained by sacrificial template method. *J Am Ceram Soc* 2021, **104**: 5679–5688.

[23] Hsiang HI, Chen CC, Yang SY. Microwave dielectric properties of $Ca_{0.7}Nd_{0.2}TiO_3$ ceramic-filled $CaO–B_2O_3–SiO_2$ glass for LTCC applications. *J Adv Ceram* 2019, **8**: 345–351.

[24] Lin SH, Lin ZQ, Chen CW. Microwave dielectric characterization of $Ca_{0.6}(La_{1-x}Y_x)_{0.2667}TiO_3$ perovskite ceramics with high positive temperature coefficient. *Ceram Int* 2021, **47**: 16828–16832.

[25] Zhou D, Pang LX, Wang DW, *et al*. High permittivity and low loss microwave dielectrics suitable for 5G resonators and low temperature co-fired ceramic architecture. *J Mater Chem C* 2017, **5**: 10094–10098.

[26] Ullah A, Liu HX, Manan A, *et al*. Microwave dielectric properties of $Bi_2(Li_{0.5}Ta_{1.5})O_7–TiO_2$-based ceramics for 5G cellular base station resonator application. *Ceram Int* 2021, **47**: 8416–8423.

[27] Pang LX, Zhou D, Qi ZM, *et al*. Structure–property relationships of low sintering temperature scheelite-structured $(1-x)BiVO_4–xLaNbO_4$ microwave dielectric ceramics. *J Mater Chem C* 2017, **5**: 2695–2701.

[28] Pang LX, Zhou D, Liu WG, *et al*. Crystal structure and microwave dielectric behaviors of scheelite structured $(1-x)BiVO_4–xLa_{2/3}MoO_4$ ($0.0 \leqslant x \leqslant 1.0$) ceramics with ultra-low sintering temperature. *J Eur Ceram Soc* 2018, **38**: 1535–1540.

[29] Chen HT, Tang B, Gao AQ, *et al*. Aluminum substitution for titanium in $Ba_{3.75}Nd_{9.5}Ti_{18}O_{54}$ microwave dielectric ceramics. *J Mater Sci Mater Electron* 2015, **26**: 405–410.

[30] Tao J, Mu ML, Wang XH, *et al*. Improved microwave dielectric properties of anti-reduction $Ba_4(Ce_{0.5}Sm_{0.5})_{9.3}Ti_{18-z}Al_zO_{54}$ ceramics sintered in nitrogen atmosphere. *J Mater Sci Mater Electron* 2018, **29**: 1392–1398.

[31] Guo X, Tang B, Liu JQ, *et al*. Microwave dielectric properties and microstructure of $Ba_{6-3x}Nd_{8+2x}Ti_{18-y}(Cr_{1/2}Nb_{1/2})_yO_{54}$ ceramics. *J Alloys Compd* 2015, **646**: 512–516.

[32] Chen HT, Tang B, Duan SX, *et al*. Microstructure and microwave dielectric properties of $Ba_{3.75}Nd_{9.5}Ti_{18-z}(Mg_{1/3}Nb_{2/3})_zO_{54}$ ceramics. *J Electron Mater* 2015, **44**: 1081–1087.

[33] Xiong Z, Tang B, Fang ZX, *et al*. Crystal structure, Raman spectroscopy and microwave dielectric properties of $Ba_{3.75}Nd_{9.5}Ti_{18-z}(Al_{1/2}Nb_{1/2})_zO_{54}$ ceramics. *J Alloys Compd* 2017, **723**: 580–588.

[34] Chen HT, Xiong Z, Yuan Y, *et al*. Dependence of microwave dielectric properties on site substitution in $Ba_{3.75}Nd_{9.5}Ti_{18}O_{54}$ ceramic. *J Mater Sci Mater Electron* 2016, **27**: 10951–10957.

[35] Tang B, Xiang QY, Fang ZX, *et al*. Microwave dielectric properties of $Ba_{3.75}Nd_{9.5}Ti_{18-z}Cr_{4z/3}O_{54}$ ceramics. *J Mater Sci Mater Electron* 2018, **29**: 535–540.

[36] Guo WJ, Zhang J, Luo Y, *et al*. Microwave dielectric properties and thermally stimulated depolarization of Al-doped $Ba_4(Sm,Nd)_{9.33}Ti_{18}O_{54}$ ceramics. *J Am Ceram Soc* 2019, **102**: 5494–5502.

[37] Wang G, Fu QY, Shi H, *et al*. Novel thermally stable, high quality factor $Ba_4(Pr_{0.4}Sm_{0.6})_{28/3}Ti_{18-y}Ga_{4y/3}O_{54}$ microwave dielectric ceramics. *J Am Ceram Soc* 2020, **103**: 2520–2527.

[38] Rodriguez-Carvajal J. *A Program for Rietveld, Profile Matching and Integrated Intensity Refinements for X-ray and Neutron Data.* Fullprof 2000, Version 1.6: Laboratoire Leon Brillouin, Gif sur Yvette, France, 2000.

[39] Hakki BW, Coleman PD. A dielectric resonator method of measuring inductive capacities in the millimeter range. *IRE Trans Microw Theory Tech* 1960, **8**: 402–410.

[40] Courtney WE. Analysis and evaluation of a method of measuring the complex permittivity and permeability microwave insulators. *IEEE Trans Microw Theory Tech* 1970, **18**: 476–485.

[41] Krupka J, Derzakowski K, Riddle B, *et al*. A dielectric resonator for measurements of complex permittivity of low loss dielectric materials as a function of temperature. *Meas Sci Technol* 1998, **9**: 1751–1756.

[42] Shannon RD. Dielectric polarizabilities of ions in oxides and fluorides. *J Appl Phys* 1993, **73**: 348–366.

[43] Pei CJ, Tan JJ, Li Y, *et al*. Effect of Sb-site nonstoichiometry on the structure and microwave dielectric properties of $Li_3Mg_2Sb_{1-x}O_6$ ceramics. *J Adv Ceram* 2020, **9**: 588–594.

[44] Xia WS, Li LX, Ning PF, *et al*. Relationship between bond ionicity, lattice energy, and microwave dielectric properties of $Zn(Ta_{1-x}Nb_x)_2O_6$ ceramics. *J Am Ceram Soc* 2012, **95**: 2587–2592.

[45] Huang FY, Su H, Li YX, *et al*. Low-temperature sintering and microwave dielectric properties of $CaMg_{1-x}Li_{2x}Si_2O_6$ (x = 0–0.3) ceramics. *J Adv Ceram* 2020, **9**: 471–480.

[46] Zhou X, Liu LT, Sun JJ, *et al*. Effects of $(Mg_{1/3}Sb_{2/3})^{4+}$ substitution on the structure and microwave dielectric properties of $Ce_2Zr_3(MoO_4)_9$ ceramics. *J Adv Ceram* 2021, **10**: 778–789.

[47] Sebastian MT. *Dielectric Materials for Wireless Communication.* Amsterdam, the Netherlands: Elsevier, 2008.

[48] Chen MY, Chia CT, Lin IN, *et al*. Microwave properties of $Ba(Mg_{1/3}Ta_{2/3})O_3$, $Ba(Mg_{1/3}Nb_{2/3})O_3$ and $Ba(Co_{1/3}Nb_{2/3})O_3$ ceramics revealed by Raman scattering. *J Eur Ceram Soc* 2006, **26**: 1965–1968.

[49] Wu SY, Li Y, Chen XM. Raman spectra of Nd/Sn cosubstituted $Ba_{6-3x}Sm_{8+2x}Ti_{18}O_{54}$ microwave dielectric ceramics. *J Appl Phys* 2004, **96**: 5683–5686.

[50] Liao Q, Li L. Structural dependence of microwave dielectric properties of ixiolite structured $ZnTiNb_2O_8$ materials: Crystal structure refinement and Raman spectra study. *Dalton Trans* 2012, **41**: 6963–6969.

[51] Yin CZ, Yu ZZ, Shu LL, *et al*. A low-firing melilite ceramic $Ba_2CuGe_2O_7$ and compositional modulation on microwave dielectric properties through Mg substitution. *J Adv Ceram* 2021, **10**: 108–119.

[52] Wang G, Fu QY, Shi H, *et al*. Suppression of oxygen vacancies generation in $Ba_{6-3x}Sm_{8+2x}Ti_{18}O_{54}$ (x = 2/3) microwave dielectric ceramics through Pr substitution. *Ceram Int* 2019, **45**: 22148–22155.

[53] Wang G, Fu QY, Guo PJ, *et al*. A/B-site cosubstituted $Ba_4Pr_{28/3}Ti_{18}O_{54}$ microwave dielectric ceramics with temperature stable and high Q in a wide range. *Ceram Int* 2020, **46**: 11474–11483.

[54] Xiong Z, Tang B, Yang CT, *et al*. Correlation between structures and microwave dielectric properties of $Ba_{3.75}Nd_{9.5-x}Sm_xTi_{17.5}(Cr_{1/2}Nb_{1/2})_{0.5}O_{54}$ ceramics. *J Alloys Compd* 2018, **740**: 492–499.

[55] Wu SY, Li Y, Chen XM. Raman spectra of $Ba_{6-3x}Sm_{8+2x}Ti_{18}O_{54}$ solid solution. *J Phys Chem Solids* 2003, **64**: 2365–2368.

[56] Scott JF, Remeika JP. High-temperature Raman study of samarium aluminate. *Phys Rev B* 1970, **1**: 4182–4185.

[57] Zaghrioui M, Bulou A, Laffez P, *et al*. Raman study of metal–insulator transition in $NdNiO_3$ thin films. *J Magn Magn Mater* 2000, **211**: 238–242.

[58] Sanjuán ML, Orera VM, Merino RI, *et al*. Raman and X-ray study of perovskite solid solutions. *J Phys*: *Condens Matter* 1998, **10**: 11687–11702.

[59] Tompsett GA, Sammes NM, Phillips RJ. Raman spectroscopy of the $LaGaO_3$ phase transition. *J Raman Spectrosc* 1999, **30**: 497–500.

[60] Loridant S, Abello L, Lucazeau G. Polarized Raman spectra of single crystals of $BaCeO_3$. *J Raman Spectrosc* 1997, **28**: 283–288.

[61] Wu MJ, Zhang YC, Xiang MQ. Synthesis, characterization and dielectric properties of a novel temperature stable $(1-x)CoTiNb_2O_8$–$xZnNb_2O_6$ ceramic. *J Adv Ceram* 2019, **8**: 228–237.

[62] Liu W, Randall CA. Thermally stimulated relaxation in Fe-doped $SrTiO_3$ systems: I. single crystals. *J Am Ceram Soc* 2008, **91**: 3245–3250.

[63] Yoon SH, Randall CA, Hur KH. Correlation between resistance degradation and thermally stimulated depolarization current in acceptor (Mg)-doped $BaTiO_3$ submicrometer fine-grain ceramics. *J Am Ceram Soc* 2010, **93**: 1950–1956.

[64] Lee H, Kim JR, Lanagan MJ, *et al*. High-energy density dielectrics and capacitors for elevated temperatures: $Ca(Zr,Ti)O_3$. *J Am Ceram Soc* 2013, **96**: 1209–1213.

[65] Zhang XH, Zhang Y, Zhang J, *et al*. Microwave dielectric

properties and thermally stimulated depolarization currents study of $(1-x)Ba_{0.6}Sr_{0.4}La_4Ti_4O_{15}$–$xTiO_2$ ceramics. *J Am Ceram Soc* 2014, **97**: 3170–3176.

[66] Zhang XH, Zhang J, Xie ZK, *et al*. Structure, microwave dielectric properties and thermally stimulated depolarization currents of $(1-x)Ba_{0.6}Sr_{0.4}La_4Ti_4O_{15}$–$xBa_5Nb_4O_{15}$ solid solutions. *J Am Ceram Soc* 2015, **98**: 1245–1252.

[67] Zhang J, Zhou YY, Peng B, *et al*. Microwave dielectric properties and thermally stimulated depolarization currents of MgF_2-doped diopside ceramics. *J Am Ceram Soc* 2014, **97**: 3537–3543.

[68] Zhang J, Yue ZX, Luo Y, *et al*. Understanding the thermally stimulated relaxation and defect behavior of Ti-containing microwave dielectrics: A case study of $BaTi_4O_9$. *Mater Des* 2017, **130**: 479–487.

[69] Luo Y, Zhang J, Yue ZX, *et al*. Improvement in microwave dielectric properties of Sr_2TiO_4 ceramics through post-annealing treatment. *J Electroceramics* 2018, **41**: 67–72.

[70] Hino T. Thermally stimulated characteristics in solid dielectrics. *IEEE Trans Electr Insul* 1980, **EI-15**: 301–311.

[71] Lee SJ, Kang KY, Han SK. Low-frequency dielectric relaxation of $BaTiO_3$ thin-film capacitors. *Appl Phys Lett* 1999, **75**: 1784–1786.

[72] Bräunlich P. *Topics in Applied Physics: Thermally Stimulated Relaxation in Solids*. Berlin, Heidelberg, Germany: Springer, 1979.

[73] Yao XG, Lin HX, Zhao XY, *et al*. Effects of Al_2O_3 addition on the microstructure and microwave dielectric properties of $Ba_4Nd_{9.33}Ti_{18}O_{54}$ ceramics. *Ceram Int* 2012, **38**: 6723–6728.

[74] An SB, Jiang J, Wang JZ, *et al*. Microwave dielectric property modification of $Ba_4Nd_{9.33}Ti_{18}O_{54}$ ceramics by the substitution of $(Al_{0.5}Nb_{0.5})^{4+}$ for Ti^{4+} and the addition of $NdAlO_3$. *Ceram Int* 2020, **46**: 3960–3967.

[75] Zhou LL, Zhou HQ, Shao H, *et al*. Microstructure and microwave dielectric properties of $Ba_{6-3x}Sm_{8+2x}Ti_{18}O_{54}$ ceramics with various $Ba_xSr_{1-x}TiO_3$ additions. *J Rare Earths* 2012, **30**: 142–145.

[76] Xu Y, Fu RL, Agathopoulos S, *et al*. Synthesis and microwave dielectric properties of BaO–Sm_2O_3–$5TiO_2$ ceramics with $NdAlO_3$ additions. *Ceram Int* 2016, **42**: 14573–14580.

[77] Xie WT, Zhang XY, Hang HC, *et al*. Microwave dielectric properties and microstructures of $xBa_{0.33}Sr_{0.67}TiO_3$–$(1-x)Ba_4Sm_{9.33}Ti_{18}O_{54}$ ceramics with near-zero temperature coefficient. *J Mater Sci Mater Electron* 2019, **30**: 4064–4068.

[78] Li LX, Wang XB, Luo WJ, *et al*. Internal-strain-controlled tungsten bronze structural ceramics for 5G millimeter-wave metamaterials. *J Mater Chem C* 2021, **9**: 14359–14370.